Supplementary Information

Grain-Boundary-Rich Cathode Enabling Fast Ion Diffusion Kinetics for Low-Temperature and High-Rate Lithium-Ion Batteries

*Fanteng Meng, [a] Yutong Li, [*b,c] Shitong Wang, [d] Dong Luo, [a] Xinghao Zhang, [b] Manfred Wagner, [e] Zilong Tang, [f] Yanpeng Li, [c] Debin Kong, [*b] and Linjie Zhi [*a,c]*

a. *School of Materials Science and Engineering, China University of Petroleum (East China), 266580, China.*

b. *Shandong Key Laboratory of Advanced Electrochemical Energy Storage Technologies, College of New Energy, China University of Petroleum (East China), 266580, China.*

c. *Advanced Chemical Engineering and Energy Materials Research Center, China University of Petroleum (East China), 266580, China.*

d. *School of Physics, Beihang University, Beijing 100191, P. R. China*

e. *Max Planck Institute for Polymer Research, Ackermannweg 10, 55128, Germany*

f. *State Key Lab of New Ceramics and Fine Processing, School of Materials Science and Engineering, Tsinghua University, Beijing 100084, P. R. China*

E-mail: zhilj@upc.edu.cn, lyt@upc.edu.cn, kongdb@upc.edu.cn

Supplementary Figures S1~S22
Supplementary Tables S1
Supplementary References 1~30

Supplementary Figures

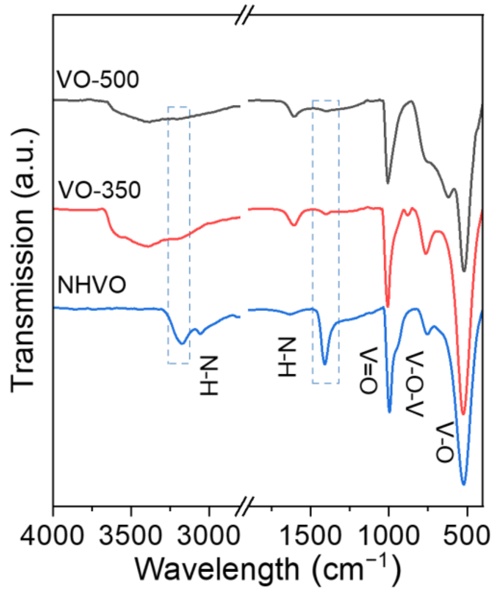

Fig. S1 Fourier transform infrared spectroscopy (FTIR) spectra of NHVO, VO-350, and VO-500.

FTIR reveal that the peak at 524 cm^{-1} corresponds to the bending vibration of V−O, while the peak at 760 cm^{-1} is assigned to the antisymmetric V−O−V stretching mode. The peak at 1000 cm^{-1} is attributed to the stretching vibration of V=O. These peaks are blue shifted during the phase transition from NHVO to VO-500, which may be attributed to the generation of lattice oxygen defects, a shortening of the V-O bond length and an increase in the bond strength. The peaks at 1408 and 3178 cm^{-1} are ascribed to the bending and stretching vibrations of N−H bonds, respectively, with peak intensity decreasing as the NH_4^+ content diminishes in VO-350 and VO-500.[1, 2]

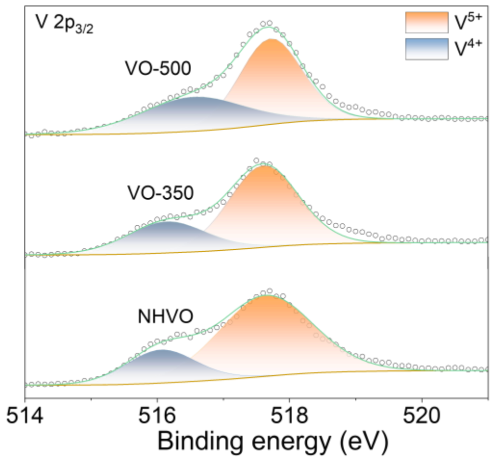

Fig. S2 V $2p_{3/2}$ X-ray photoelectron spectroscopy (XPS) spectra of NHVO, VO-350, and VO-500.

The high-resolution V $2p_{3/2}$ spectra indicate that the relative area of the V^{5+} peak decreases from NHVO to VO-500, while the V^{4+} peak increases, reflecting a reduction in the valence state of vanadium during the phase transition. This is attributed to the gradual phase transition process from $NH_4V_4O_{10}$ (with an average vanadium valence of +4.75) to V_6O_{13} (with an average vanadium valence of +4.33).[3]

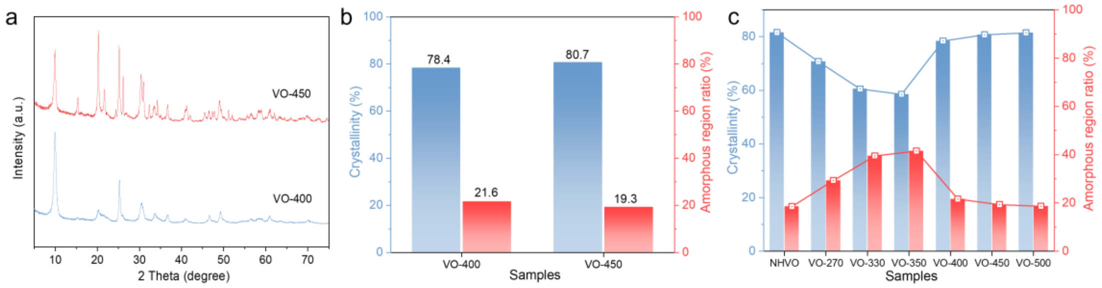

Fig. S3 (a) XRD patterns and (b) crystallinity and amorphous region ratio of VO-400 and VO-450. (c) The variation trends of crystallinity and amorphous region content in all samples. The crystallinity values of VO-400 and VO-450 samples are 78.4% and 80.7%, with corresponding amorphous region proportions of 21.6% and 19.3%, respectively. It can be observed that when the temperature reaches the high-temperature range of 400 °C and above, the material's crystallinity significantly improves, which can be attributed to crystal rearrangement and grain growth.

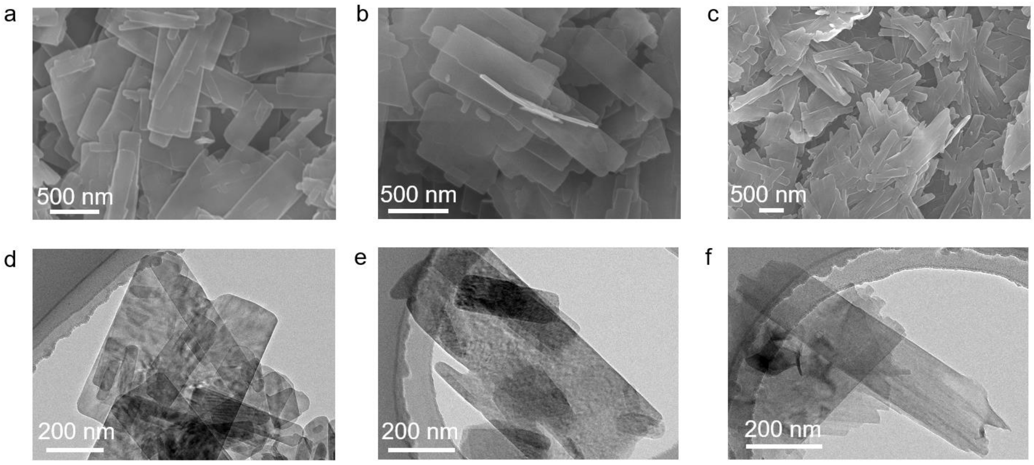

Fig. S4 SEM images of (a) NHVO, (b) VO-350, and (c) VO-500. TEM images of (d) NHVO, (e) VO-350, and (f) VO-500.

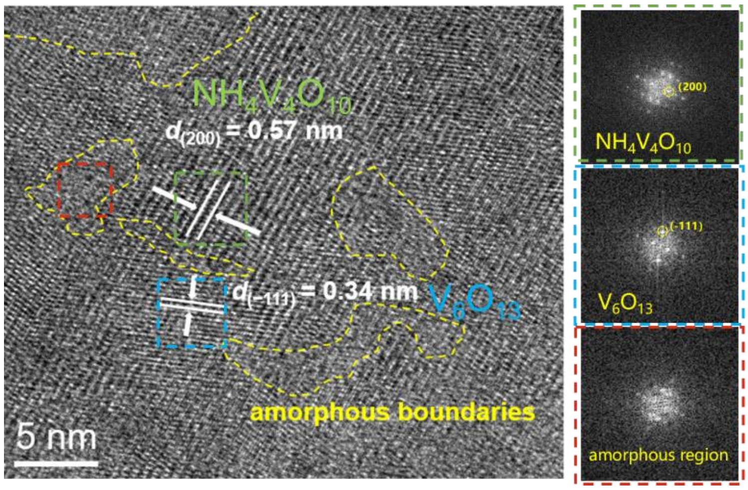

Fig. S5 HRTEM image of VO-350 and the corresponding SAED patterns of the selected regions.

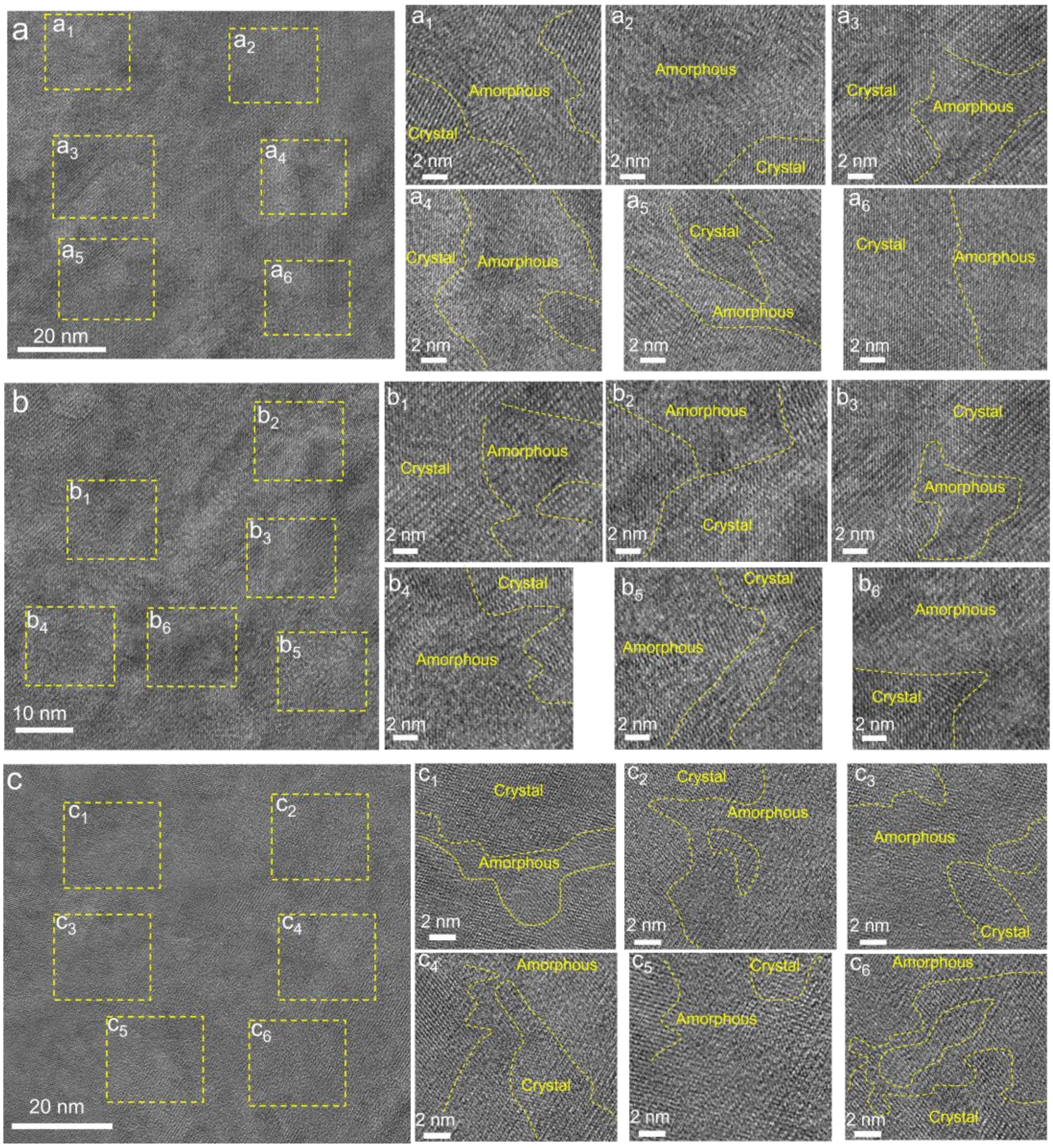

Fig. S6 (a-c) HRTEM images of the grain-boundary-rich cathode (VO-350).

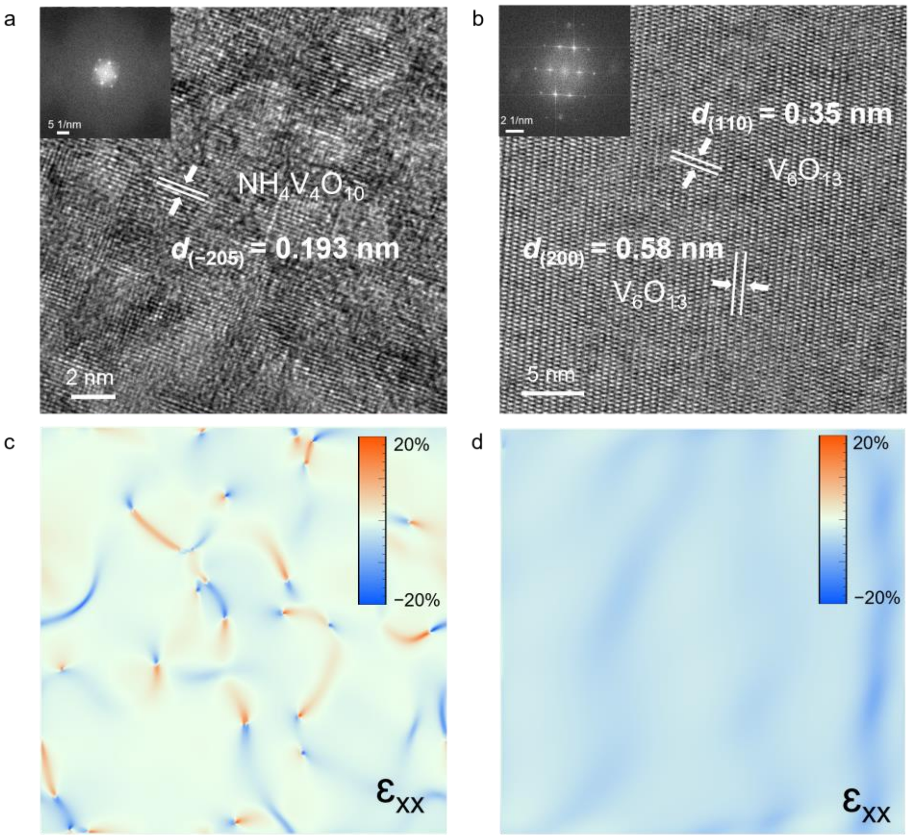

Fig. S7 HRTEM (inset is the corresponding SAED pattern) images of (a) NHVO and (b) VO-500. (c) Strain distributions corresponding to (a) and (d) strain distributions corresponding to (b) (blue and orange-red represent compressive strain and tensile strain, respectively).

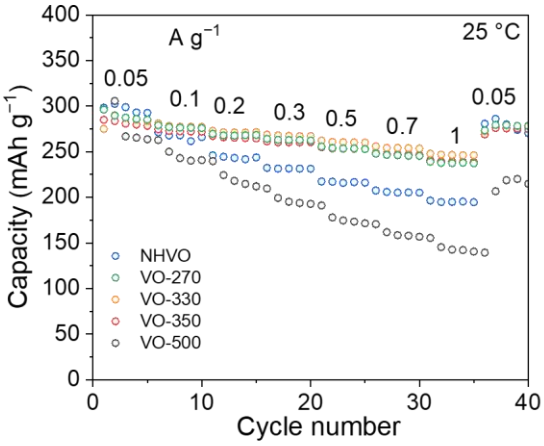

Fig. S8 Rate performance of NHVO, VO-270, VO-330, VO-350, and VO-500 at 25 °C.

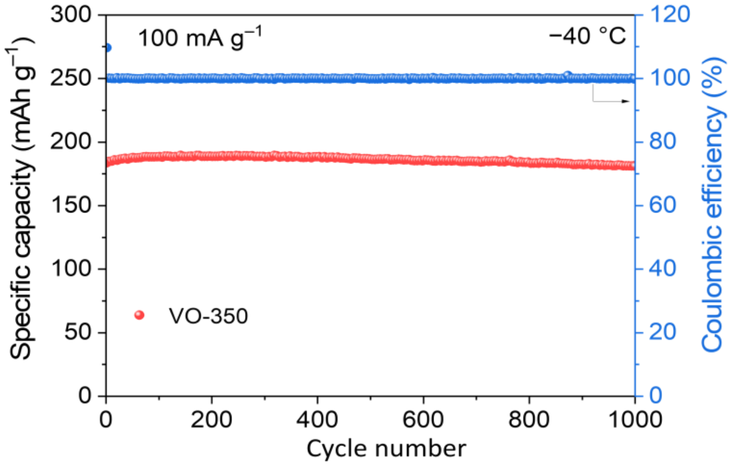

Fig. S9 Cycling performance of VO-350 at 100 mA g^{-1} and −40 °C.

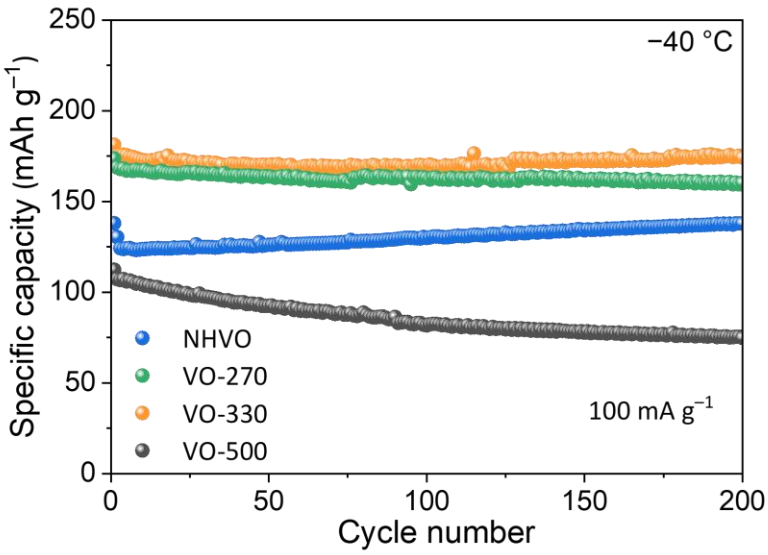

Fig. S10 Cycling performance of NHVO, VO-270, VO-330, and VO-500 at 100 mA g^{-1} and −40 °C.

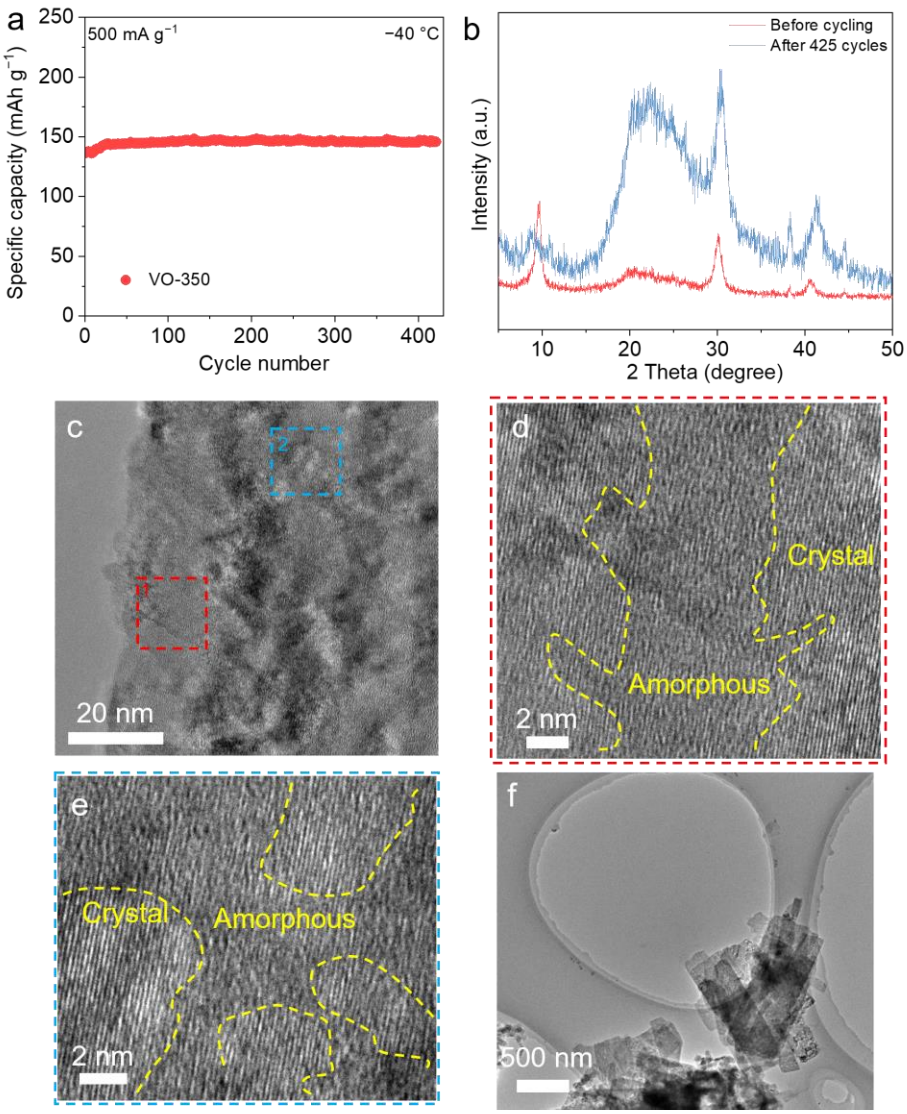

Fig. S11 (a) Long cycle performance of VO-350 at −40 °C and 500 mA g^{-1}. (b) XRD pattern of VO-350 after 425 cycles at −40 °C. (b) HRTEM image of VO-350 after 425 cycles. (d) Enlarged HRTEM image of VO-350 for selected region 1 in (c). (e) Enlarged HRTEM image of VO-350 for selected region 2 in (c). (f) TEM image of VO-350 after 425 cycles.

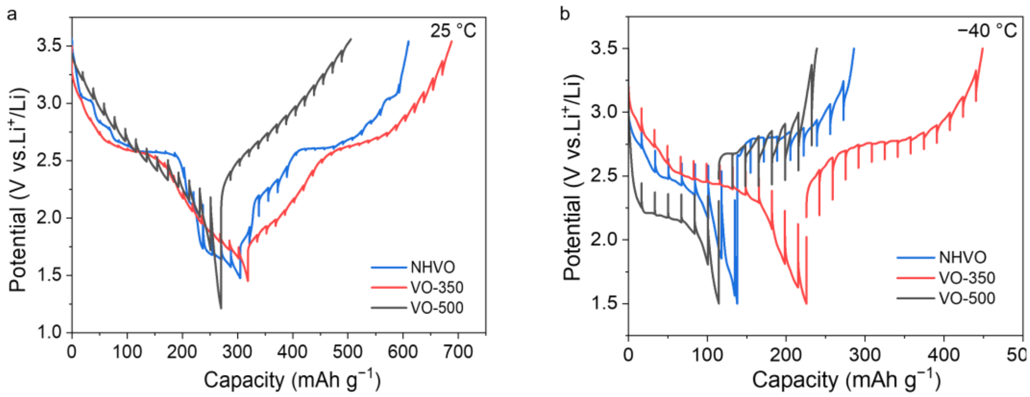

Fig. S12 GITT plots of NHVO, VO-350, and VO-500 at (a) 25 °C and (b) −40 °C.

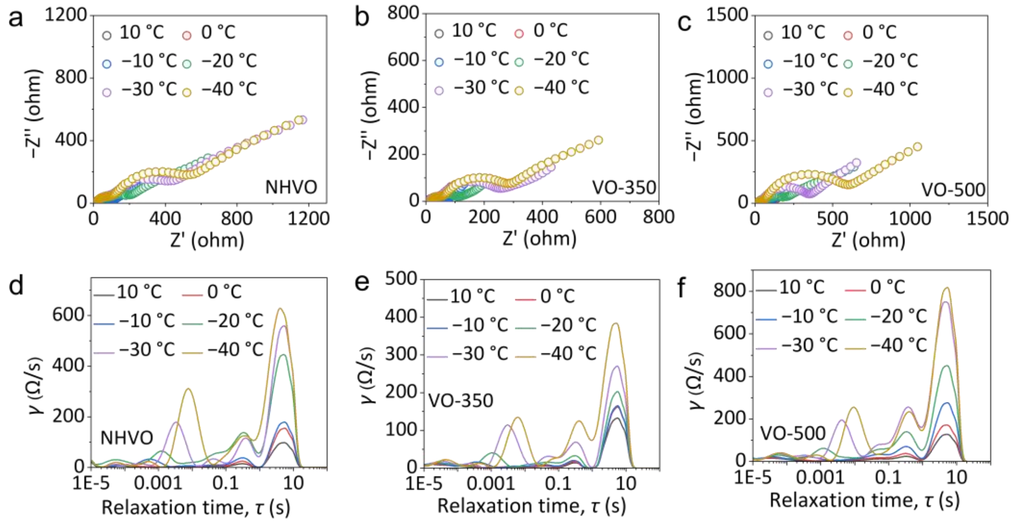

Fig. S13 (a-c) EIS plots at various temperatures and (d-f) corresponding DRT results of NHVO, VO-350, and VO-500.

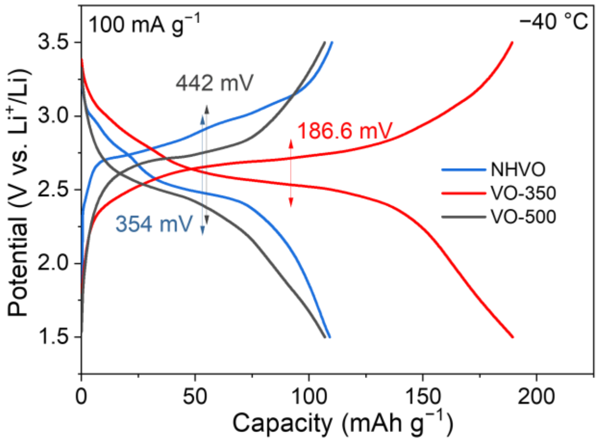

Fig. S14 GCD plots of NHVO, VO-350, and VO-500 at −40 °C.

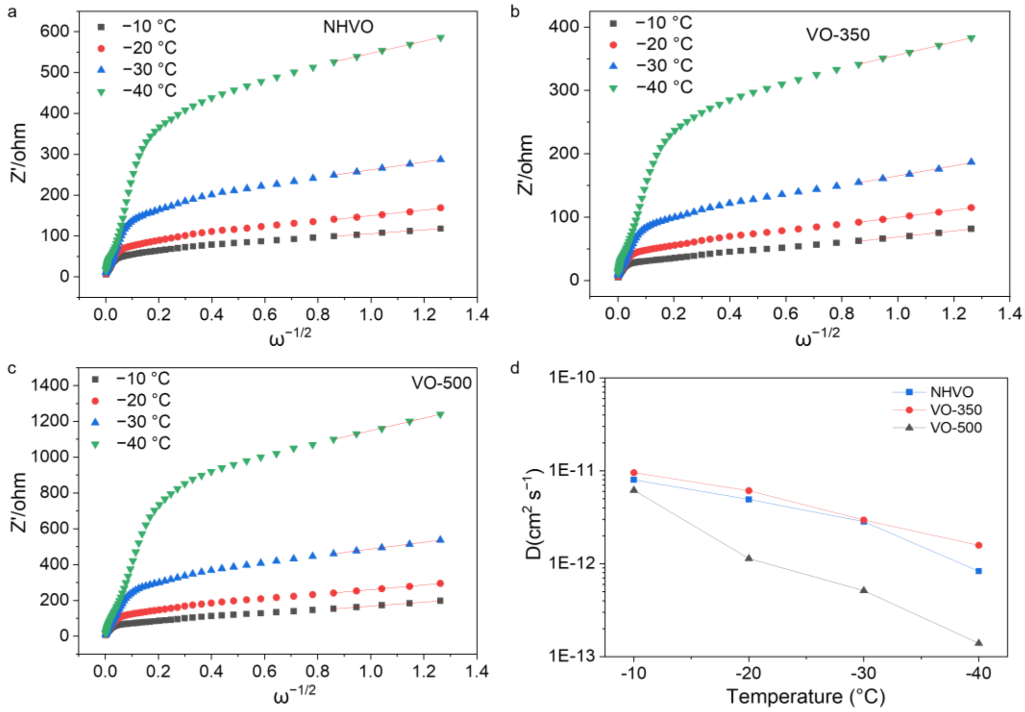

Fig. S15 Relationship between Z' and $\omega^{-1/2}$ of (a) NHVO, (b) VO-350, and (c) VO-500. (d) Li^+ diffusion coefficients at different temperatures of NHVO, VO-350, and VO-500.

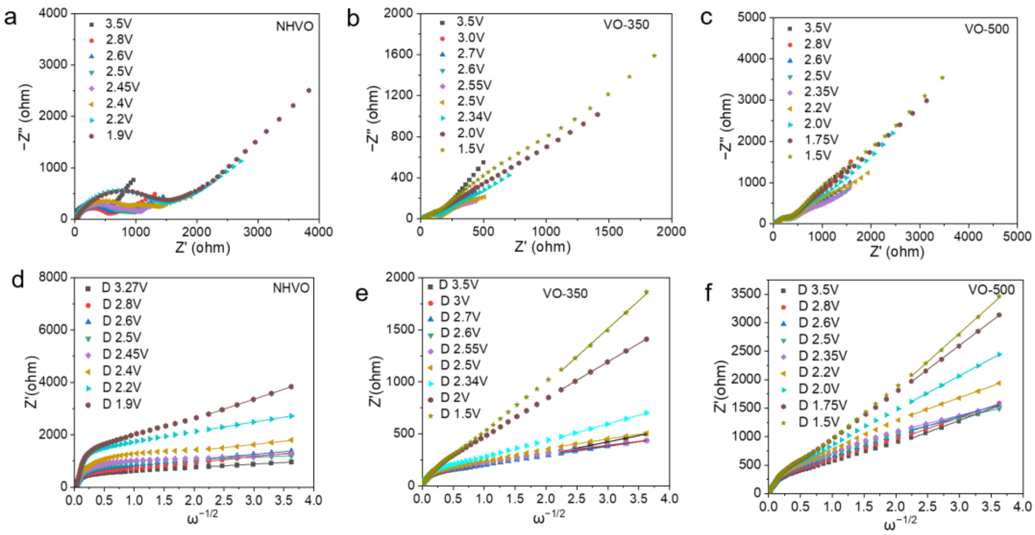

Fig. S16 In situ EIS evolution of (a) NHVO, (b) VO-350, and (c) VO-500 during the discharge process at −40 °C. Relationship between Z' and $\omega^{-1/2}$ of (d) NHVO, (e) VO-350, and (f) VO-500 at different discharge states.

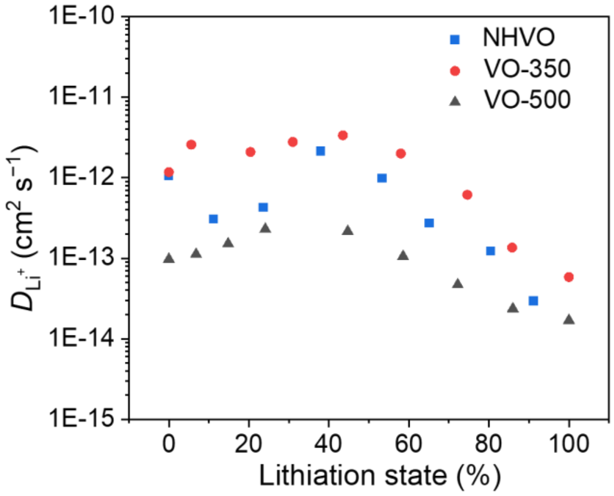

Fig. S17 Li^+ diffusion coefficients of NHVO, VO-350, and VO-500 during the discharge process at −40 °C.

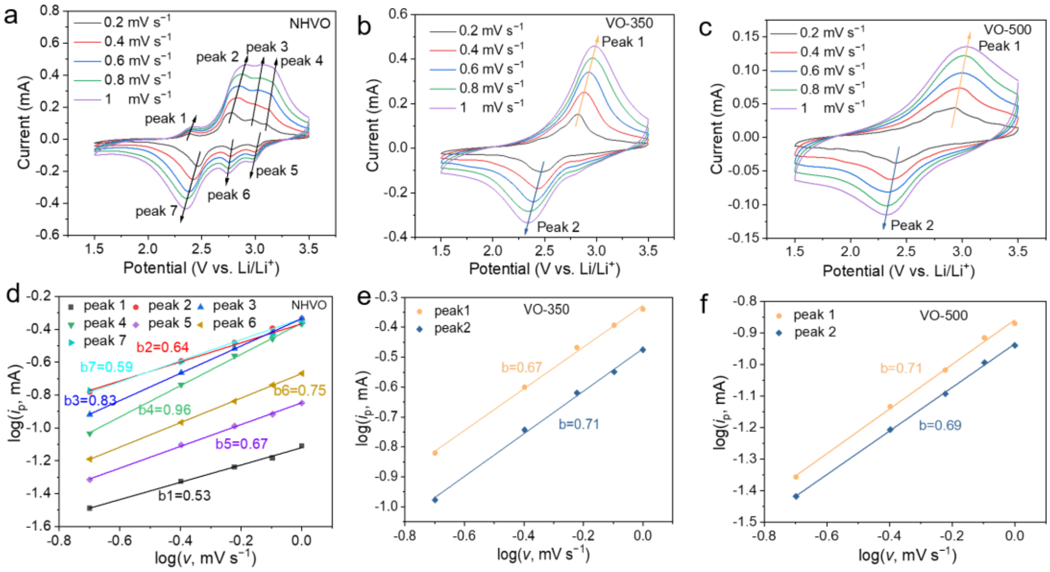

Fig. S18 CV curves at different scan rates of (a) NHVO, (b) VO-350, and (c) VO-500. Determination of the b values of (d) NHVO, (e) VO-350, and (f) VO-500 using the relationship between peak current and scan rate.

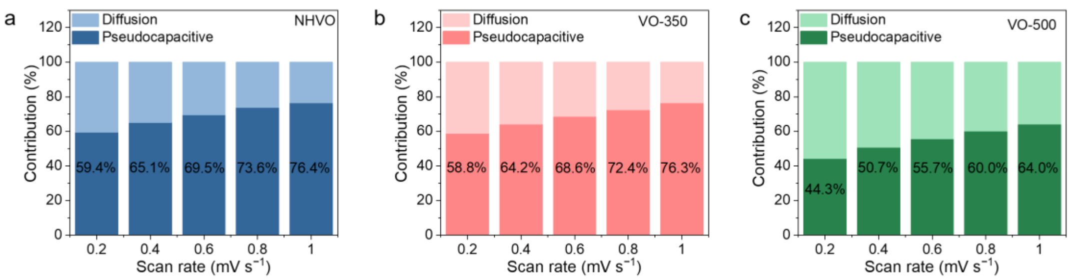

Fig. S19 Contribution ratios of pseudocapacitive at different scan rates of (a) NHVO, (b) VO-350, and (c) VO-500.

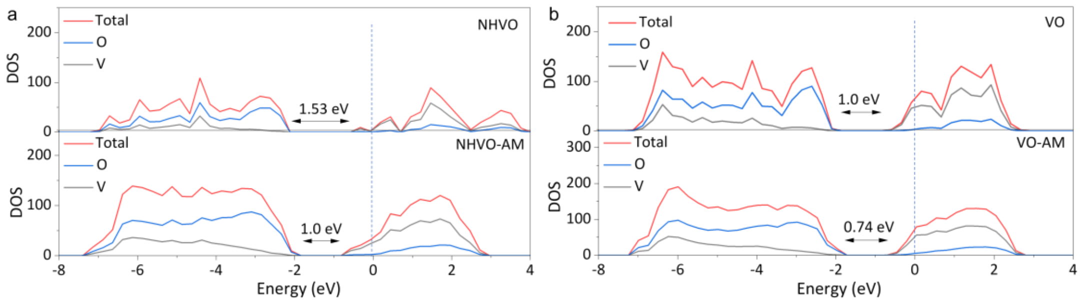

Fig. S20 (a) DOS calculations for NHVO and NHVO-AM. (b) DOS calculations for VO and VO-AM.

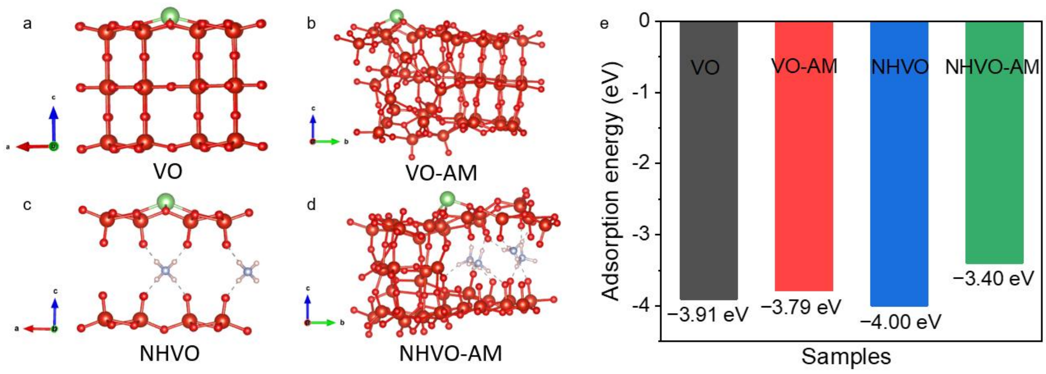

Fig. S21 (a-d) Adsorption models and (e) adsorption energy of Li^{+} on the surface of VO, VO-AM, NHVO, and NHVO-AM.

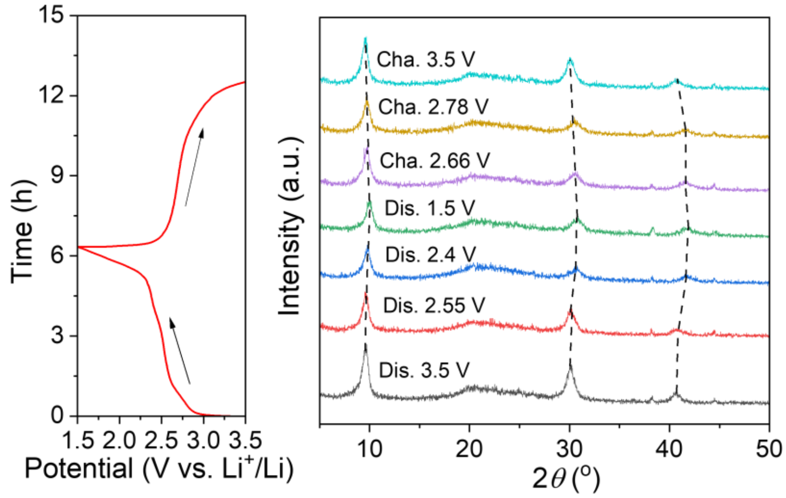

Fig. S22 Ex-situ XRD analysis of VO-350 during the discharge and charge processes at −40 °C.

Supplementary Table

Table S1. Comparison of low-temperature performance between VO-350 and reported cathodes.

Cathode	Temperature	Current density	Capacity (mAh g^{-1})	Capacity retention	Reference
VO-350	−40 °C	0.17 C (1 C = 300 mA g^{-1})	203 mAh g^{-1}	72.5%	This work
	−40 °C	0.33 C (1 C = 300 mA g^{-1})	186 mAh g^{-1}	68.3%	
	−40 °C	1 C (1 C = 300 mA g^{-1})	151.5 mAh g^{-1}	58.2%	
	−40 °C	1.67 C (1 C = 300 mA g^{-1})	133.6 mAh g^{-1}	52.7%	
	−40 °C	3.33 C (1 C = 300 mA g^{-1})	104.8 mAh g^{-1}	44%	
	−50 °C	0.17 C (1 C = 300 mA g^{-1})	189 mAh g^{-1}	63%	
	−60 °C	0.17 C (1 C = 300 mA g^{-1})	154 mAh g^{-1}	51.2%	
$LiNi_{0.5}Mn_{1.5}O_4$	−20 °C	0.1 C (1 C = 146.7 mA g^{-1})	82.24 mAh g^{-1}	61 %	4
$LiNi_{0.5}Mn_{1.5}O_4$	−30 °C	0.1 C (1 C = 150 mA g^{-1})	83.1 mAh g^{-1}	63.8 %	5
$LiNi_{0.5}Mn_{1.5}O_4$	−30 °C	0.25C (1 C = 148 mA g^{-1})	60 mAh g^{-1}	53.6 %	6
$LiNi_{0.5}Mn_{1.5}O_4$	−20 °C	1C (1 C = 148 mA g^{-1})	32 mAh g^{-1}	26.7 %	7
NCM622	−60 °C	1/15 C	90 mAh g^{-1}	45%	8
NCM333@LBO	−40 °C	0.2C	101.9 mAh g^{-1}	57.8%	9
NCM811	−40 °C	0.1 C	150 mAh g^{-1}	74%	10
LCO	−60 °C	0.1 C	60.6 mAh g^{-1}	46%	11
$LiFePO_4$/C	−20 °C	0.1C (1 C = 170 mA g^{-1})	130 mAh g^{-1}	78 %	12
LFP/CNT	−25 °C	0.2C (1 C = 170 mA g^{-1})	121 mAh g^{-1}	71.4%	13
LFP	−30 °C	0.1C (1 C = 170 mA g^{-1})	78.2 mAh g^{-1}	51.5%	14
LFP	−40 °C	0.1C (1 C = 170 mA g^{-1})	87 mAh g^{-1}	56%	15
$LiMn_{0.8}Fe_{0.2}PO_4$/C	−15 °C	0.1C (1 C = 170 mA g^{-1})	97 mAh g^{-1}	64%	16
LVP/C	−20 °C	0.1C	118.9 mAh g^{-1}	63.4%	17
r-LVP	−30 °C	0.2 C (1 C = 130 mA g^{-1})	90 mAh g^{-1}	80%	18
β-$Li_xV_2O_5$	−40 °C	0.1 C	123.8 mAh g^{-1}	60%	19
3S-V_2O_5-HMSs	25 °C	1000 mA g^{-1}	402.4 mAh g^{-1}	/	20
THS-V_2O_5	25 °C	1600 mA g^{-1}	330 mAh g^{-1}	/	21
V_2O_5-300	−40 °C	100 mA g^{-1}	189 mAh g^{-1}	74%	22
400-V_2O_5	25 °C	150 mA g^{-1}	170.1 mAh g^{-1}	/	23
VO_2F	25 °C	1C (1C=262 mA g^{-1})	150 mAh g^{-1}	/	24
V_2O_5 sheets	25 °C	1C (1C=294 mA g^{-1})	172 mAh g^{-1}	/	25
$V_2O_5 \cdot nH_2O$/rGO	25 °C	1000 mA g^{-1}	196 mAh g^{-1}	/	26
V_2O_5-HMs	25 °C	1C (1C=147 mA g^{-1})	145.3 mAh g^{-1}	/	27

FeVO NSs	25 °C	100 mA g^{-1}	273 mAh g^{-1}	/	28
vanadium oxide PNSs	25 °C	100 mA g^{-1}	220 mAh g^{-1}	/	29
vanadium pentoxide	25 °C	100 mA g^{-1}	150 mAh g^{-1}	/	30

Supplementary References

1 Q. Zong, Q. Wang, C. Liu, D. Tao, J. Wang, J. Zhang, H. Du, J. Chen, Q. Zhang and G. Cao, *ACS Nano*, 2022, **16**, 4588-4598.

2 Y. Li, S. Wang, Y. Dong, Y. Yang, Z. Zhang and Z. Tang, *Adv. Energy Mater.*, 2020, **10**, 1903411.

3 Z. Wang, Y. Song, J. Wang, Y. Lin, J. Meng, W. Cui and X.-X. Liu, *Angew. Chem. Int. Ed.*, 2023, **62**, e202216290.

4 K. Bi, S.-X. Zhao, C. Huang and C.-W. Nan, *J. Power Sources*, 2018, **389**, 240-248.

5 D. Guan, J. Zeng, Z. Xue, Y. Cao, G. Hu, Z. Peng and K. Du, *ACS Appl. Energy Mater.*, 2023, **6**, 9568-9576.

6 G. A. Elia, F. Nobili, R. Tossici, R. Marassi, A. Savoini, S. Panero and J. Hassoun, *J. Power Sources*, 2015, **275**, 227-233.

7 Y.-C. Jin, M.-I. Lu, T.-H. Wang, C.-R. Yang and J.-G. Duh, *J. Power Sources*, 2014, **262**, 483-487.

8 Y. Yang, Y. Yin, D. M. Davies, M. Zhang, M. Mayer, Y. Zhang, E. S. Sablina, S. Wang, J. Z. Lee, O. Borodin, C. S. Rustomji and Y. S. Meng, *Energy Environ. Sci.*, 2020, **13**, 2209-2219.

9 S. Tan, L. Wang, L. Bian, J. Xu, W. Ren, P. Hu and A. Chang, *J. Power Sources*, 2015, **277**, 139-146.

10 J. Holoubek, K. Kim, Y. Yin, Z. Wu, H. Liu, M. Li, A. Chen, H. Gao, G. Cai, T. A. Pascal, P. Liu and Z. Chen, *Energy Environ. Sci.*, 2022, **15**, 1647-1658.

11 C. S. Rustomji, Y. Yang, T. K. Kim, J. Mac, Y. J. Kim, E. Caldwell, H. Chung and Y. S. Meng, *Science*, 2017, **356**, eaal4263.

12 F. Zheng, C. Yang, X. Ji, D. Hu, Y. Chen and M. Liu, *J. Power Sources*, 2015, **288**, 337-344.

13 X.-L. Wu, Y.-G. Guo, J. Su, J.-W. Xiong, Y.-L. Zhang and L.-J. Wan, *Adv. Energy Mater.*, 2013, **3**, 1155-1160.

14 B. Wu, Y. Ren, D. Mu, X. Liu, G. Yang and Z. Sun, *Solid State Ionics*, 2014, **260**, 8-14.

15 B. Yao, Z. Ding, J. Zhang, X. Feng and L. Yin, *J. Solid State Chem.*, 2014, **216**, 9-12.

16 W. Yang, Y. Bi, Y. Qin, Y. Liu, X. Zhang, B. Yang, Q. Wu, D. Wang and S. Shi, *J. Power Sources*, 2015, **275**, 785-791.

17 Y. Q. Qiao, J. P. Tu, X. L. Wang and C. D. Gu, *J. Power Sources*, 2012, **199**, 287-292.

18 R. Qin, Y. Wei, T. Zhai and H. Li, *J. Mater. Chem. A*, 2018, **6**, 9737-9746.

19 P.-P. Wang, C.-Y. Xu, W.-D. Li, L. Wang and L. Zhen, *Electrochim. Acta*, 2015, **169**, 440-446.

20 J. Wang, H. Tang, L. Zhang, H. Ren, R. Yu, Q. Jin, J. Qi, D. Mao, M. Yang, Y. Wang, P. Liu, Y. Zhang, Y. Wen, L. Gu, G. Ma, Z. Su, Z. Tang, H. Zhao and D. Wang, *Nat. Energy*, 2016, **1**, 16050.

21 C. Wang, L. Zhang, M. Al-Mamun, Y. Dou, P. Liu, D. Su, G. Wang, S. Zhang, D. Wang and H. Zhao, *Adv. Energy Mater.*, 2019, **9**, 1900909.

22 F. Meng, Y. Li, Y. Liu, S. Zhang, D. Kong and L. Zhi, *Adv. Funct. Mater.*, 2025, 2419994.

23 D. Lee, H. Lee, Y.-T. Kim, K. Lee and J. Choi, *Electrochim. Acta*, 2020, **330**, 135192.

24 M. A. Cambaz, B. P. Vinayan, O. Clemens, A. R. Munnangi, V. S. K. Chakravadhanula, C. Kübel and M. Fichtner, *Inorg. Chem.*, 2016, **55**, 3789-3796.

25 H. Wu, M. Qin, X. Li, Z. Cao, B. Jia, Z. Zhang, D. Zhang, X. Qu and A. A. Volinsky, *Electrochim. Acta*, 2016, **206**, 301-306.

26 Y. Zhang, X. Yuan, T. Lu, Z. Gong, L. Pan and S. Guo, *J. Colloid Interface Sci.*, 2021, **585**, 347-354.

27 P. Zhang, L. Zhao, Q. An, Q. Wei, L. Zhou, X. Wei, J. Sheng and L. Mai, *Small*, 2016, **12**, 1082-1090.

28 Q. Wei, Q. Wang, Q. Li, Q. An, Y. Zhao, Z. Peng, Y. Jiang, S. Tan, M. Yan and L. Mai, *Nano Energy*, 2018, **47**, 294-300.

29 Q. Wei, S. Tan, X. Liu, M. Yan, F. Wang, Q. Li, Q. An, R. Sun, K. Zhao, H. Wu and L. Mai, *Adv. Funct. Mater.*, 2015, **25**, 1773-1779.

30 Q. An, Q. Wei, P. Zhang, J. Sheng, K. M. Hercule, F. Lv, Q. Wang, X. Wei and L. Mai, *Small*, 2015, **11**, 2654-2660.